

A Z-Scheme Heterojunctional Photocatalyst Engineered with Spatially Separated Dual Redox Sites for Selective CO₂ Reduction with Water: Insight by In Situ μ s-Transient Absorption Spectra

Ling Sun, Ziqing Zhang, Ji Bian,* Fuquan Bai, Hengwei Su, Zhijun Li, Jijia Xie, Rongping Xu, Jianhui Sun, Linlu Bai, Cailing Chen, Yu Han, Junwang Tang,* and Liqiang Jing*

Solar-driven CO₂ reduction by water with a Z-scheme heterojunction affords an avenue to access energy storage and to alleviate greenhouse gas (GHG) emissions, yet the separation of charge carriers and the integrative regulation of water oxidation and CO₂ activation sites remain challenging. Here, a BiVO₄/g-C₃N₄ (BVO/CN) Z-scheme heterojunction as such a prototype is constructed by spatially separated dual sites with CoO_x clusters and imidazolium ionic liquids (IL) toward CO₂ photoreduction. The optimized CoO_x-BVO/CN-IL delivers an \approx 80-fold CO production rate without H₂ evolution compared with urea-C₃N₄ counterpart, together with nearly stoichiometric O₂ gas produced. Experimental results and DFT calculations unveil the cascade Z-scheme charge transfer and subsequently the prominent redox co-catalysis by CoO_x and IL for holes-H₂O oxidation and electrons-CO₂ reduction, respectively. Moreover, in situ μ s-transient absorption spectra clearly show the function of each cocatalyst and quantitatively reveal that the resulting CoO_x-BVO/CN-IL reaches up to the electron transfer efficiency of 36.4% for CO₂ reduction, far beyond those for BVO/CN (4.0%) and urea-CN (0.8%), underlining an exceptional synergy of dual reaction sites engineering. This work provides deep insights and guidelines for the rational design of highly efficient Z-scheme heterojunctions with precise redox catalytic sites toward solar fuel production.

1. Introduction

The worldwide energy crisis and climate changes triggered by the over emission of CO₂ have raised ever-growing concerns. To achieve CO₂ fixation with renewable energy by sustainable and green technologies provides an alternative route to tackle the aforesaid matters. Photocatalytic CO₂ reduction, driven by inexhaustible solar energy, has been deemed as one of the tempting avenues to realize carbon-neutral energy circulation by converting CO₂ into value-added fuels and chemicals.^[1–2] In this context, tremendous efforts have been devoted to the design and seeking of photocatalytic nanomaterials for highly-efficient solar-driven CO₂ reduction.^[3,4] Among diverse photocatalysts explored up to date, graphitic carbon nitride (CN) is emerging as an appealing candidate with the merits of negatively-positioned conduction band (CB) and benign visible-light absorption characters, etc.^[5,6] However, the current CO₂ conversion performance

L. Sun, Z. Zhang, J. Bian, Z. Li, R. Xu, J. Sun, L. Bai, L. Jing
 Key Laboratory of Functional Inorganic Materials Chemistry
 (Ministry of Education)
 School of Chemistry and Materials Science
 International Joint Research Center and Lab for Catalytic Technology
 Heilongjiang University
 Harbin 150080, P. R. China
 E-mail: bianji@hlju.edu.cn; jinglq@hlju.edu.cn
 F. Bai, H. Su
 International Joint Research Laboratory
 of Nano-Micro Architecture Chemistry
 Institute of Theoretical Chemistry
 Jilin University
 Changchun 130021, P. R. China

J. Xie, J. Tang
 Department of Chemical Engineering
 University College London
 Torrington Place, London WC1E 7JE, UK
 E-mail: junwang.tang@ucl.ac.uk
 C. Chen, Y. Han
 Advanced Membranes and Porous Materials Center
 Physical Science and Engineering Division
 King Abdullah University of Science and Technology (KAUST)
 Thuwal 23955–6900, Saudi Arabia
 J. Tang
 Industrial catalysis center
 Department of Chemical Engineering
 Tsinghua University
 Beijing 100084, P. R. China

 The ORCID identification number(s) for the author(s) of this article can be found under <https://doi.org/10.1002/adma.202300064>.

DOI: 10.1002/adma.202300064

acquired on CN-based photocatalysts is still moderate, for which deep reasons mainly lie in the shallow valence band (VB) and the slow water oxidation kinetics.^[7] In recent years, integrating reductive photocatalyst (RP) CN with an oxidative photocatalyst (OP) to construct a bioinspired artificial Z-scheme heterojunction is a potential strategy to address the obstacle, and the fabricated CN-based Z-scheme heterojunctions have shown promising activities in aqueous CO₂ reduction.^[8,9] However, a great deal of effort is currently directed to optimizing the oxidation constituents of Z-scheme heterojunctions and to introduce catalytic sites for CO₂ reduction unilaterally.^[10,11]

Recent research has implied that BiVO₄, Fe₂O₃, PDI, etc. semiconductors hold great superiority to be integrated with CN as ideal OPs due to the deep valence band and the staggered energy band alignments.^[12,13] Specifically, morphology-tailored BiVO₄ nanosheet (BVO) with outstanding water oxidation properties and robust stability makes it a preferable candidate to couple with CN and to be a prototype for the exploration of such manipulation strategy on CN-based Z-scheme heterojunctions.^[14,15] Whereas, it is worth noting that the charge transfer and separation in such a Z-scheme heterojunction is still inevitable accompanied by the possible pathway that electrons transfer from RP to OP, while in parallel holes transfer from OP to RP, resembling what happens in a type II heterojunction. In this case, it would be adverse to the photocatalytic activities due to the decreased thermodynamic redox potentials of photogenerated charge carriers. Based on this view, to strengthen Z-scheme charge transfer by inhibiting the type II one is imperative for greatly maintaining sufficient redox potentials. As for this, it has recently been demonstrated that the introduced (001)-exposed TiO₂ onto CN as the energy platform prolongs the lifetimes of separated electrons and holes of the fabricated Z-scheme heterojunction with greatly-improved CO₂ photoreduction activity in the absence of cocatalysts.^[14] Water-involved CO₂ reduction process includes CO₂ reduction and water oxidation two half-reactions, and great efforts have been naturally devoted to the former one for a long time,^[16] while the latter one is exactly quite a sluggish procedure in the overall CO₂ reduction reactions. Hence, it is meaningful to modulate photogenerated holes of OP to facilitate water oxidation for effective Z-scheme charge transfer, unfortunately, it has seldom been investigated.

Obviously, it is vital to take into account water oxidation activation as well as CO₂ reduction one simultaneously on the basis of the manipulated cascade Z-scheme heterojunction. In this regard, to introduce redox catalytic sites, especially for spatially separated ones on the RP and OP precisely, is critical for the overall artificial photosynthesis. Nevertheless, constructing such ingenious CN-based Z-scheme heterojunctions from the perspective of these two aspects has barely been investigated in the reported examples yet, while remains challenging. Targeted co-catalyst engineering is extremely important not only for the capture of charge carriers but also for the promotion of surface reaction kinetics. To date, representative Co oxides species remain one of the most effective cocatalysts capable of trapping photogenerated holes and lowering the energy barrier of water oxidation in photoelectrocatalysis and photocatalysis.^[17,18] In general, CoO_x with tunable Co³⁺/Co²⁺ ratios stands out and has been approved to be beneficial for creating intended *OOH

intermediates hence facilitating water activation markedly.^[19] To maximize the catalytic site and maintain high atom utilization efficiency, scaling CoO_x into nanoclusters and anchoring it on the OP of fabricated BVO/CN Z-scheme heterojunction is anticipated to greatly extract holes and then accelerate the kinetics of water oxidation half-reaction, meanwhile prolonging the electron lifetime of CN. In this consideration, the precise regulation of CoO_x clusters on BVO is important for the directional charge transfer in the Z-scheme heterojunction. Whereas, it is difficult to tailor the deposition of cocatalyst on the desirable BVO accurately in such a heterojunction system. It was once reported that Ag and MnO_x could be selectively deposited on the anisotropic facets of BiVO₄ based on the discrepancy between electrons and holes accumulation characters on different crystal facets,^[20] for achieving the cocatalysts with spatial separation to promote water oxidation and hence improve the efficiency of overall water splitting. Inspired by this thought, it is quite feasible to anchor CoO_x clusters on BVO by an in situ deposition process with the spatially separated photoholes under Z-scheme charge transfer. Thus, it is expected that the electron lifetime of CN could be prolonged by precisely engineering CoO_x clusters on BVO to modulate holes as marked water-oxidation co-catalysts.

Besides, to directionally introduce an active cocatalyst for CO₂ reduction is also crucial to take advantage of the long-lived electrons in CN. Despite several cocatalysts like MXene, MOFs and transition metal atoms, etc. have shown great success in catalyzing CO₂ reduction,^[21,22] most of the studies focus more on the aspects of enlarging the surface areas to promote CO₂ adsorption and lower the energy barriers for CO₂ activation. Nevertheless, to create a microenvironment for CO₂ enrichment and to build an intimate connection between cocatalysts and photocatalysts would be the key foundation for CO₂ activation. Therefore, it is of great significance to seek a brand-new family of materials for photocatalysis as the new generation cocatalysts with three merits: i) desirable CO₂ affinity to concentrate and activate CO₂, ii) abundant surface functionalities to establish effective interfacial linkage with a used photocatalyst, and iii) favorable charge transfer and transportation. Ionic liquids (IL), a category of organic salts that are formed by a weak interaction of organic cations and charge-delocalized inorganic/organic anions, feature noteworthy properties of high ionic conductivity, acceptable biocompatibility, and solvation power.^[23,24] Thus, the premier application of IL is devoted to electrochemical investigation as electrolytes and materials synthesis, etc.^[25] With the rapid exploration of IL in fields of catalytic conversion, imidazolium IL has been determined to endow with the nature of high capability for CO₂ capture.^[26] In addition, it has been demonstrated that imidazolium IL served as a cocatalyst in electrochemistry and could lower the potential for formation of CO₂⁻ intermediates so as to promote the CO₂ conversion rate and then improve Faradaic efficiencies. Similar findings on IL with the function of CO₂ activation have also been disclosed in electrocatalytic CO₂ reduction for the past few years widely.^[27] Of note, the C(2)-H in imidazole ring tends to complex with CO₂ instead of H₂O hence to inhibit the competitive hydrogen evolution and being conducive to CO₂ reduction.^[28] Intriguingly, the imidazolium ring holds benign linkage sites for the connection with nanomaterials by H-bonding interactions,

which would provide opportunities for its precise decoration on CN for CO₂ adsorption and activation in photocatalysis at the aid of static electricity attraction.^[29] Accordingly, it is reasoned that CO₂ photoreduction performance of CN-based Z-scheme heterojunctions could be greatly boosted synergistically by targeted engineering of spatially-separated CoO_x clusters and IL respectively to modulate charges with redox co-catalysis. However, the use of imidazolium IL in photoreduction of CO₂ has far less been explored, and the limited investigation of such a strategy has been reported to date in detail.

The current explorations on mechanism of Z-scheme heterojunctions have tended to figure out the charge transfer pathway between the employed two constituents, whether from the view of experimental or theoretical aspects.^[30] However, the deep mechanism insight on charge modulation and catalytic process of proposed Z-scheme charge transfer remains unclear yet. To gain key information on how modified CoO_x clusters and IL work efficiently on the designed heterojunction, it is imperative to track the in-depth understanding of the dynamics of charge transfer and the involved catalytic process during CO₂ reduction with in situ time-resolved techniques. Transient absorption spectroscopy (TAS) as an advanced technique has widely been employed to unravel the charge carrier dynamics of solid semiconductors in photocatalytic water splitting and H₂ evolution.^[31] Specifically, it is more reasonable to distinguish the charge transfer and induced redox reactions from the perspective of matched time threshold with μs-TAS. Interestingly based on the quantitatively evaluated electron transfer efficiency (ETE) for CO₂ reduction, it can give overwhelming support to elucidate charge carriers dynamic behavior and the catalytic process by in situ TAS investigation under identical conditions in CO₂ reduction process. Importantly, it will lay the foundation for clarifying the intrinsic synergy between charge extraction and co-catalysis on a Z-scheme heterojunction with in situ circumstances, potentially guiding the rational design of desirable photocatalysts toward CO₂ photoreduction, as yet related studies have rarely been reported.

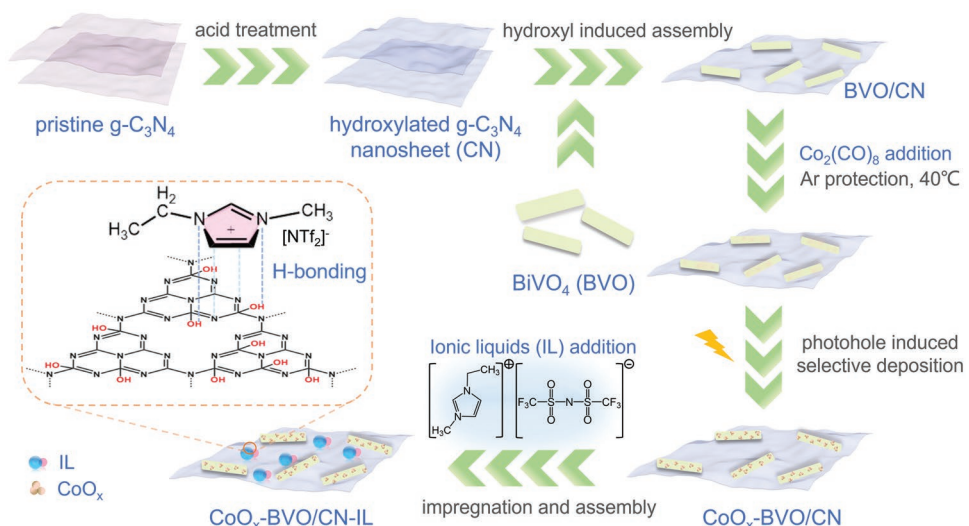
Herein, BVO/CN Z-scheme nanosheet heterojunction as such a proof-of-concept prototype has been successfully

manipulated by spatially separated dual sites engineering for photocatalytic CO₂ reduction by pure water. The CO₂ conversion has been substantially boosted due to i) the promoted Z-scheme charge transfer, ii) the modulated co-catalysis from the anchored CoO_x clusters for capturing holes and then accelerating water oxidation dynamics, and iii) the modified IL for activating CO₂, which is unveiled by experimental results and DFT calculations comprehensively. Moreover, as disclosed by *in situ* TAS, the optimal CoO_x-BVO/CN-IL reaches up to the ETE of 36.4% for CO₂ reduction, far beyond those for BVO/CN, CoO_x-BVO/CN, and BVO/CN-IL, highlighting the synergy of long-lived electron lifetime and the effective catalysis brought by the rational design of Z-scheme heterojunction and precise construction of co-catalysis sites. Significantly, the proposed strategy has also been demonstrated to improve the CO₂ reduction on other CN-based Z-scheme heterojunctions (eg. WO₃/CN and α-Fe₂O₃/CN). This work proposes a new avenue for the construction of heterojunctional catalysts toward CO₂ conversion with high efficiency from the perspective of charge extraction and precise engineering of spatially separated redox sites.

2. Results and Discussion

2.1. Controlled Synthesis and Structure Characterization

The design and controlled synthesis process of CoO_x-BVO/CN-IL was presented in Scheme 1. Starting from the pristine g-C₃N₄ synthesized by a molecule self-assembly method with melamine and cyanuric acid as raw materials,^[32] CN was endowed with abundant hydroxyl groups via post-treatment with acid. Subsequently, the resulting CN was integrated with a pre-prepared BVO nanosheet by a hydroxyl-induced assembly. On the basis of fabricated BVO/CN nanosheet heterojunction, CoO_x nanoclusters were directionally anchored on BVO through the photogenerated hole-assisted selective deposition with Co₂(CO)₈ as the cobalt source at first, and then IL 1-ethyl-3-methyl-imidazolium bis(trifluoromethylsulfonyl)imide ([Emim][NTf₂]) was



Scheme 1. Schematic illustration of the design and controlled synthesis process of spatially separated CoO_x and IL-modified BVO/CN (CoO_x-BVO/CN-IL).

controllably decorated on CN by impregnation and the following H-bond induced assembly procedure. It is worth noting that to increase the amount of surface hydroxyl groups of CN for the targeted combination of CN and IL is crucial to create spatially separated active sites of IL and CoO_x nanoclusters.

As depicted in X-ray diffraction (XRD) patterns (Figures S1 and S2, Supporting Information), a weak and broad peak at (002) is detected for CN.^[33] A series of diffraction peaks assigned to monoclinic BiVO_4 (JCPDS PDF no. 14–0688) could be seen on BVO/CN heterojunctions,^[34] while the absence of CoO_x characteristic diffraction peak in $\text{CoO}_x\text{-BVO}/\text{CN}$ is probably caused by the tiny amount with high dispersion and the ultrafine size. As expected, further introduction of IL does not influence the crystal structure of resulting heterojunction. The ultraviolet-visible diffuse reflectance spectra (DRS) disclose that the optical absorption edge of CN is located at approximately ≈ 450 nm, and an additional absorption edge at ≈ 550 nm emerges after coupling with BVO, indicating the successful hybridization of BVO and CN (Figure S3, Supporting Information). While the CoO_x decoration and subsequent IL modification have a neglectable impact on the light absorption of BVO/CN. Based on the transmission electron microscopy (TEM) images shown in Figure S4 (Supporting Information), it is confirmed that the CN shows a sheet-like structural feature. Turning to $\text{CoO}_x\text{-BVO}/\text{CN}$, BVO with the nanobelt morphology is closely attached on CN, in which the mean width of

50 nm and the length range from 250 to 300 nm are observed (Figure S5, Supporting Information). Not any additional nanoparticles assigned to CoO_x could be seen for $\text{CoO}_x\text{-BVO}/\text{CN}$ in the TEM image, while the energy-dispersive X-ray (EDX) elemental mapping shows the homogeneous distribution of C, N, Bi, V, Co, and O elements (Figure S6, Supporting Information). It is noticed that the morphology $\text{CoO}_x\text{-BVO}/\text{CN}$ is retained after subsequent IL decoration (Figure S7, Supporting Information), whereas under aberration-corrected high-angle annular dark-field scanning TEM (AC HAADF-STEM) image, highly dispersed sub-nanoscaled CoO_x clusters are resolved on BVO (Figure 1a). In addition, the element mapping manifests the uniform distribution of C, N, Bi, V, Co, O, and F elements, indicative of the uniform introduction of IL (Figure 1b).

According to X-ray photoelectron spectroscopy (XPS) depicted in Figure S8 (Supporting Information), the binding energies of C 1s and N 1s in BVO/CN have a positive shift in comparison with those of CN, while the Bi 4f and V 2p XPS peaks shift to a lower binding energy compared with BVO (Figure S9, Supporting Information). This is related to the Fermi level equilibrium between BVO and CN when these two constituents come into close integration. For $\text{CoO}_x\text{-BVO}/\text{CN}$ one, the N 1s spectrum (Figure S10, Supporting Information) could be further fitted with three peaks located at 398.6, 399.7, and 401.0 eV, which are assigned to C=N=C, N-(C)₃, and C-NH, respectively.^[35] Based on an additional peak ascribed to

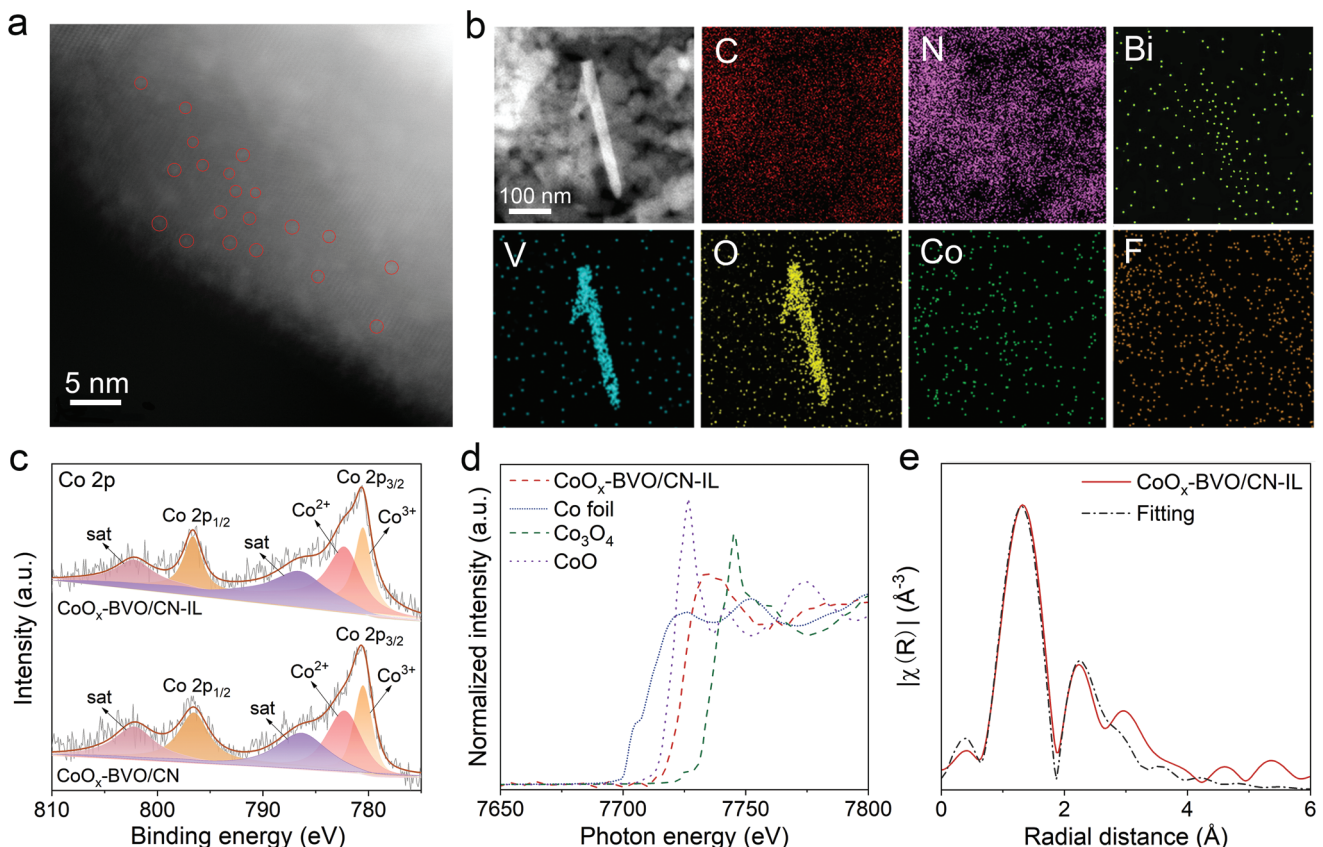


Figure 1. a) AC-STEM image of $\text{CoO}_x\text{-BVO}/\text{CN-IL}$, b) High-angle annular dark-field scanning TEM image of $\text{CoO}_x\text{-BVO}/\text{CN-IL}$ and the corresponding EDX mapping images of elemental C, N, Bi, V, O, Co and F, c) XPS analyses of Co 2p for $\text{CoO}_x\text{-BVO}/\text{CN}$ and $\text{CoO}_x\text{-BVO}/\text{CN-IL}$, d) Co K-edge XANES profiles of Co foil, CoO, Co_3O_4 , and $\text{CoO}_x\text{-BVO}/\text{CN-IL}$, e) Fitting curves for Co K-edge EXAFS spectra of $\text{CoO}_x\text{-BVO}/\text{CN-IL}$.

the $[\text{NTf}_2]^-$ after IL introduction and the detected F element in XPS survey of $\text{CoO}_x\text{-BVO/CN-IL}$ (Figure S11, Supporting Information),^[36] it is confirmed that IL has indeed been modified on the heterojunction. On the other hand, the binding energy of sp^2 -hybridized carbon of triazine ring ($\text{N}-\text{C}=\text{N}$) detected on $\text{CoO}_x\text{-BVO/CN-IL}$ exhibits a positive shift compared with that of $\text{CoO}_x\text{-BVO/CN}$ (Figure S12, Supporting Information).^[37] In combination with the fact that the surface hydroxyl groups of CN are greatly increased after HNO_3 treatment (Figure S13, Supporting Information), it is deduced there would mainly be an H-bond linked interaction between the N atom in imidazole ring of IL and hydroxyl groups grafted on the C atoms of CN, as well as a weak interaction between the N atoms of CN and H atoms of imidazole ring.^[29] As shown in Figure 1c, the main peaks located at ≈ 781.5 and 797.5 eV are associated with the $\text{Co } 2\text{p}_{3/2}$ and $\text{Co } 2\text{p}_{1/2}$, respectively,^[38] and they could be further deconvoluted with five peaks. The peaks located at 781.9 and 779.5 eV are assigned to Co (II) and Co (III) oxidation states, respectively.^[39] The satellite peaks centered at 786.3 and 802.9 eV are also the fingerprint of a Co (II) oxidation state.^[40] Notably, there is no visible binding energy change of Co species after introducing IL, demonstrating IL has not influenced the chemical environment of CoO_x nanoclusters in the heterojunction due to the spatially separated engineering of CoO_x and IL. The specific chemical states of Co species were further ascertained by X-ray absorption near-edge structure (XANES) profiles. Figure 1d shows the normalized Co K-edge XANES spectra with Co foil, CoO , and Co_3O_4 as references. The near-edge absorption energy for detected CoO_x falls in the range between those of CoO and Co_3O_4 , indicating positive oxidation states of Co, which is between Co (II) and Co (III). The Fourier-transformed cobalt K-edge extended X-ray absorption fine structure (EXAFS) spectra of $\text{CoO}_x\text{-BVO/CN-IL}$ were further carried out. Figure 1e and Table S1 (Supporting Information) present the fitting results. The first shell peak of the investigated sample is positioned ≈ 1.44 Å (phase-shift not corrected), which is assigned to Co–O scattering path.^[41] Meanwhile, the peak of Co–Co in $\text{CoO}_x\text{-BVO/CN-IL}$ is inconsistent with the case of Co-foil.^[40] In combination with the Co K-edge XANES edge position, it is confirmed that the cobalt species in the prepared heterojunction are ultrafine clusters with Co oxidation states, between Co (II) and Co (III).

2.2. Photocatalytic Activities and Charge Transfer and Separation

The photocatalytic performance for CO_2 reduction of as-fabricated samples was evaluated, along with the typical urea- C_3N_4 as the reference. As shown in Figure 2a, CO , CH_4 , and H_2 as the reduction products are detected. The photocatalytic activity of CN is greatly improved after integration with BVO, and the optimal loading amount is proved to be 50 wt.% (Figure S14, Supporting Information). A much higher CO_2 conversion rate is achieved after CoO_x decoration, and the optimized $\text{CoO}_x\text{-BVO/CN}$ heterojunction by altering the CoO_x loadings (Figure S15, Supporting Information) delivers a 10-fold increase in CO production over CN. However, a certain amount of H_2 was still produced. Of note, the photoactivity of $\text{CoO}_x\text{-BVO/CN}$ is

even much higher than BVO/CN-IL. Interestingly, $\text{CoO}_x\text{-BVO/CN-IL}$ with the optimal CoO_x and IL loadings gives the highest CO production rate ($83.5 \mu\text{mol g}^{-1} \text{ h}^{-1}$) and $\approx 100\%$ selectivity to carbon products. The catalyst exhibits a 20-fold and an 80-fold enhancement in CO conversion over CN and urea- C_3N_4 , respectively, comparing favorably to those of Z(S)-scheme heterojunctions reported recently (Figure S16 and Table S2, Supporting Information). One can notice that H_2 is not detected on IL-modified samples, implying the introduced IL could restrict the competitive H_2 evolution from water reduction and be conducive to the selectivity for CO_2 reduction. Besides, a certain amount of oxidation product oxygen has also been detected in course of CO_2 reduction for all heterojunctions, and it is close to the stoichiometric value (reduction products: oxygen ratio = 0.87:1) for the optimized sample. Additionally, the resulting photocatalyst ($\text{CoO}_x\text{-BVO/CN-IL}$ as a representative here) keeps unchanged CO and CH_4 production rates across four runs, manifesting it is stable during the reaction (Figure S17, Supporting Information).

Moreover, ^{13}C labeled isotopic experiment was adopted to affirm the carbon source in the reduction products (Figure 2b; Figure S18, Supporting Information). The detected peaks at $m/z = 29$ and $m/z = 17$ strongly prove that the produced CO and CH_4 are from CO_2 conversion driven by photocatalysis, rather than the decomposition of CN. It is noted that when CoO_x and IL are introduced onto BVO/pristine g- C_3N_4 heterojunction using the identical method with that of $\text{CoO}_x\text{-BVO/CN-IL}$, in which pristine g- C_3N_4 is not treated with HNO_3 in advance (denoted as $\text{CoO}_x\text{-BVO/C}_3\text{N}_4\text{-IL}$ here), the photocatalytic activity is far lower than that of $\text{CoO}_x\text{-BVO/CN-IL}$ (Figure S19, Supporting Information). This implies the modified IL is not well interacted with g- C_3N_4 due to the amount-limited hydroxyl groups. In addition, we also decorated CoO_x on BVO/CN heterojunction by a facile oxidation method and then introduced IL (detailed synthesis procedure is shown in supporting information), the obtained activity is dramatically decreased (Figure S20, Supporting Information), which is probably because that the CoO_x nanoclusters are connected with the modified IL partially. The above results strongly prove that the precise introduction of spatially separated CoO_x and IL is quite crucial for tailoring the photoactivities of BVO/CN Z-scheme heterojunction. As shown in Figure S21 (Supporting Information), the photoluminescence (PL) intensity of CN is quenched after coupling with BVO, indicating the charge recombination of CN is effectively inhibited. A much weaker PL signal is observed on $\text{CoO}_x\text{-BVO/CN}$ heterojunction compared with BVO/CN one. In comparison, the PL intensity for $\text{CoO}_x\text{-BVO/CN}$ is slightly quenched after IL introduction. What's more, the fluorescence (FS) spectra related to the formed hydroxyl radical amounts were also conducted to analyze the charge separation in fabricated heterojunctions (Figure S22, Supporting Information). The amounts of formed hydroxyl radicals are quantified by adding the probe molecule coumarin to generate the luminescent 7-hydroxy coumarin molecules. The higher FS intensity means better charge separation. One can readily see BVO/CN exhibits a stronger FS signal than pristine CN, and as expected, the FS intensity is further strengthened after CoO_x modification, evidencing the modified CoO_x could effectively facilitate the charge transfer and separation in the heterojunction. The

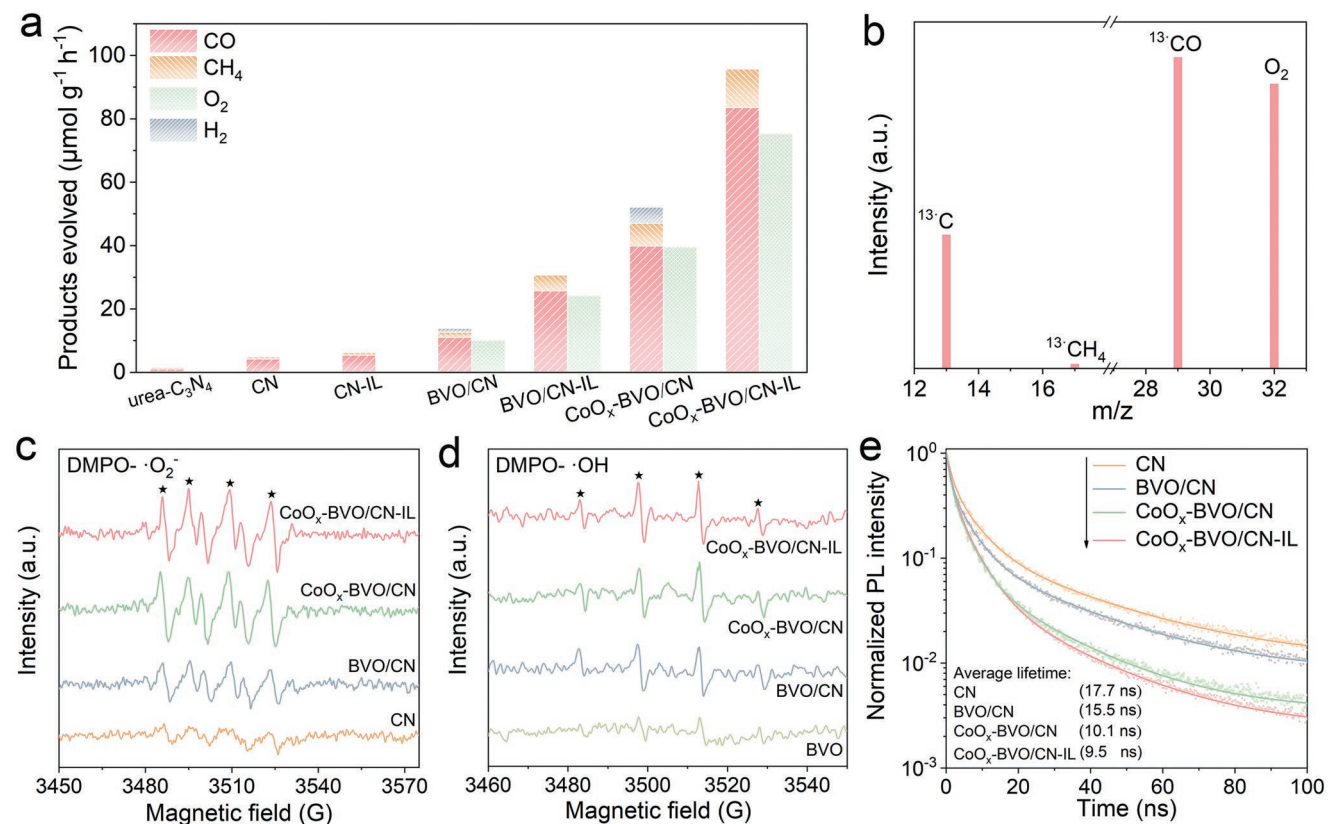


Figure 2. a) Photocatalytic activities of CO₂ reduction for a series of samples under light irradiation, b) Mass spectra of the products from the photocatalytic reduction of ¹³CO₂ over CoO_x-BVO/CN-IL. DMPO spin-trapping EPR spectra recorded for •O₂⁻ c) and •OH d) under light irradiation for CN, BVO, CoO_x-BVO/CN, and CoO_x-BVO/CN-IL. Detection conditions: the concentration of DMPO is 50 mmol L⁻¹. •O₂⁻ and •OH were determined in methanolic solution and aqueous phase, respectively. e) Time-resolved PL spectra of CN, BVO/CN, CoO_x-BVO/CN, and CoO_x-BVO/CN-IL.

recorded FS signal of CoO_x-BVO/CN-IL is a little stronger than that of CoO_x-BVO/CN, hinting the modified IL has a somewhat positive influence on charge separation, which is consistent with the PL results.

To reveal the mechanism of enhanced charge transfer and separation, electron paramagnetic resonance (EPR) spectra were first carried out (Figure 2c,d). A quartet signal of DMPO-•O₂⁻ with the intensity ratio of 1:1:1:1 is recorded on CN, and it is much stronger for BVO/CN heterojunction, while no EPR signal could be detected on bare BVO. These results strongly validate the Z-scheme charge transfer between CN and BVO, since the CB of CN could fulfill the thermodynamic requirement for the standard potential of O₂/•O₂⁻ (-0.33 V vs NHE), whereas that of BVO would not. The CB levels of BVO and CN were experimentally confirmed by Mott-Schottky (MS) curves, in which the CB bottoms of BVO and CN are determined to be -0.04 and -1.19 V versus NHE, respectively (Figures S23 and S24, Supporting Information), and the calculated energy band alignments of BVO and CN are depicted in Figure S25 (Supporting Information). Notably, the DMPO-•O₂⁻ signal on CoO_x-BVO/CN is much stronger than that of BVO/CN, while the further modification of IL has somewhat increase at the EPR signal. As anticipated, the DMPO-•OH signal is strengthened after CoO_x decoration greatly. All these results unambiguously signify the decorated CoO_x nanoclusters strongly steer the cascade Z-scheme charge transfer and

separation between BVO and CN, which is further supported by the time-resolved PL spectra. As illustrated in Figure 2e, the average PL lifetime of CN and BVO/CN are calculated to be 17.7 and 15.5 ns, respectively. A much shorter PL lifetime (10.1 ns) is observed for CoO_x-BVO/CN, and it is the shortest PL lifetime (9.5 ns) for CoO_x-BVO/CN-IL. In comparison, it is noticed that the effect of CoO_x modification is much more obvious than that with IL one. It is acceptable that the shortened PL lifetime of CN in the fabricated BVO/CN-based heterojunction clearly confirms the promoted Z-scheme charge transfer and separation after modification with CoO_x and IL.

In situ irradiated XPS analyses were employed to give more direct evidence for the charge transfer behavior across heterointerfaces. As seen in Figure 3a, the characteristic N 1s binding energy of BVO/CN heterojunction is observed to undergo negative shifts under light irradiation, suggesting an increase in its electron density. In contrast, the V 2p peak shifts to a higher binding energy, corresponding to a decrease in the electron density on BVO (Figure 3b). The observed binding energy variations provide direct evidence for the Z-scheme charge migration pathway across the BVO/CN interface, namely, the photoelectrons migrate from BVO to CN. Interestingly, the scale of both N 1s and V 2p shifts on CoO_x-BVO/CN heterojunction is more obvious than those of BVO/CN under light illumination compared with those in dark (Figure 3c,d). The result well proves the Z-scheme charge transfer of BVO/CN could be

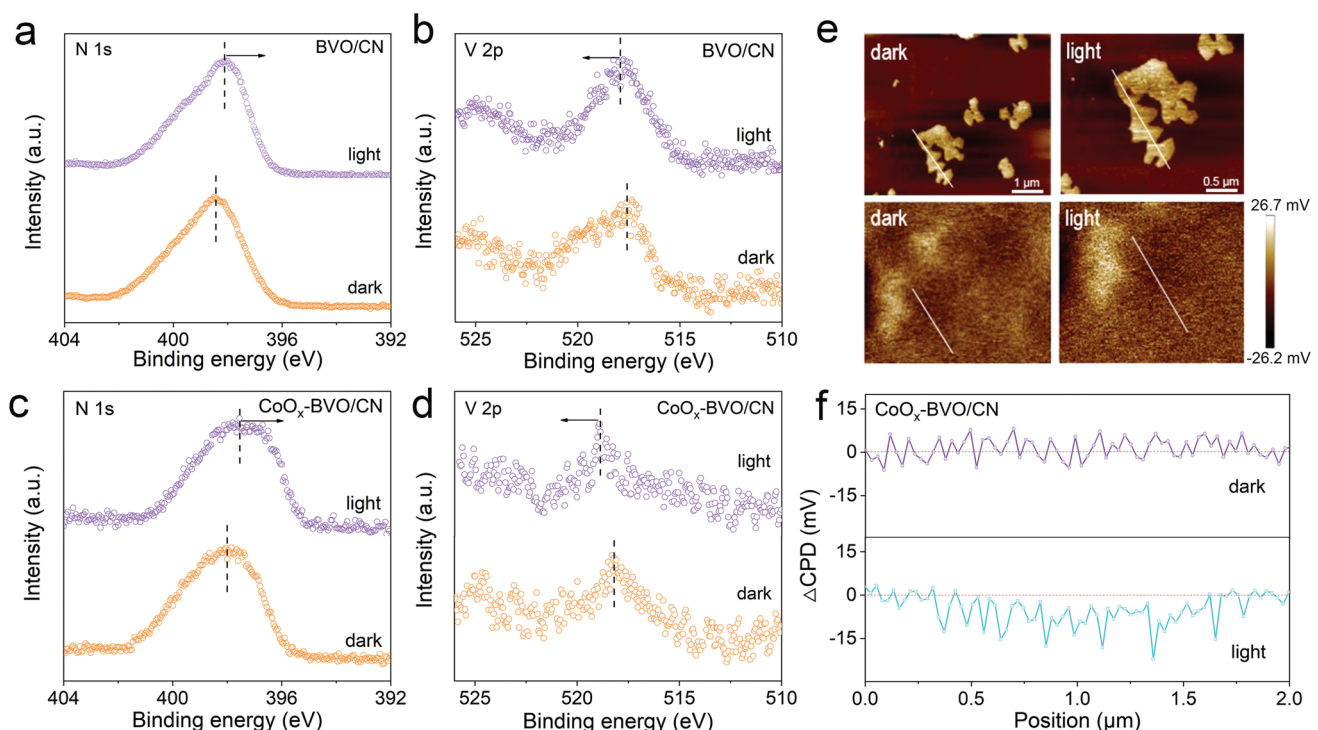


Figure 3. XPS analyses for N 1s and V 2p of BVO/CN a,b) and CoO_x-BVO/CN c,d) in the dark and under 405 nm irradiation. e) Topography and KPFM images of CoO_x-BVO/CN in the dark and under 405 nm irradiation and the corresponding contact potential differences (f).

manipulated by the anchored CoO_x clusters on BVO distinctly. This finding was further supported by Kelvin probe force microscopy (KPFM) characterizations at the nanometer scale to qualitatively map the role of CoO_x for steering Z-scheme charge transfer. The topography and the corresponding surface potential images of CN are depicted in Figure S26 (Supporting Information). It is noticed that the surface potential change could be hardly observed on CN upon light illumination due to the sluggish charge separation, and the detected contact potential difference (CPD) of BVO/CN heterojunction under light illumination is reduced by 5 mV (Figure S27, Supporting Information), indicating the photogenerated electron accumulation in CN. Surprisingly, the CPD detected on CoO_x-BVO/CN heterojunction exhibits a much obvious decrease change of 15 mV after light irradiation (Figure 3e,f), which vividly reflects the positive impact of the anchored CoO_x nanoclusters on the Z-scheme charge transfer between BVO and CN.

2.3. DFT Calculations

The effects of modified CoO_x clusters and IL on the charge transfer and separation of BVO/CN Z-scheme heterojunction were further supported by the first principles and quantum dynamics calculations. Figure 4a depicts the interfacial geometries (left) and the hole locations after the electron transfer processes (right) of CoO_x-BVO. A stable CoO_x-BVO model is obtained with a weak binding that is established between the Co atom and O atom of BVO. One can see the photogenerated holes are accumulated in the CoO_x moiety of the model

under the excitation state, and the charge distribution has not changed after the introduction of CN (Figure 4b). The overall charge injection characters for CoO_x-BVO and CoO_x-BVO/CN are substantially maintained. It could be pointed out here that the charge transfer pathway is prominently prolonged after introducing CN, while the holistic charge transfer at the interface for both CoO_x-BVO and CoO_x-BVO/CN basically complete within 300 fs (Figure 4c), implying the modified CoO_x could effectively extract the photogenerated holes of BVO and thus facilitate the charge transfer in the Z-scheme heterojunction. The crucial role of IL in the charge separation of BVO/CN Z-scheme heterojunction was further revealed. Figure 4d describes the interfacial geometries (left) and the electronic population after the electron transfer processes (right) of BVO/CN. It can be seen that the electrons are accumulated on the CN part of the BVO/CN heterojunction after excitation. By comparison, the electrons exhibit a concussive characteristic in the inner two layers of CN after further introducing IL, which could be explained by the shielding effect caused by the π-π interaction (3.06 Å) between the outer layer of CN and IL (Figure 4e; Figure S28, Supporting Information). Note that the overall charge transfer amounts for BVO/CN and BVO/CN-IL are comparative, involving 50 fs at an ultrafast timescale, the discrepancy of the charge transfer character for BVO/CN and BVO/CN-IL is quite small (Figure 4f). Furthermore, the excited-state interfacial electron transfer process of BVO/CN and BVO/CN-IL is elaborately disclosed fundamentally with the introduction of CO₂. For BVO/CN, the electron accumulation feature on CN is more obvious than the case without CO₂ (Figure 4g and Figure S29, Supporting Information). Surprisingly, the electron

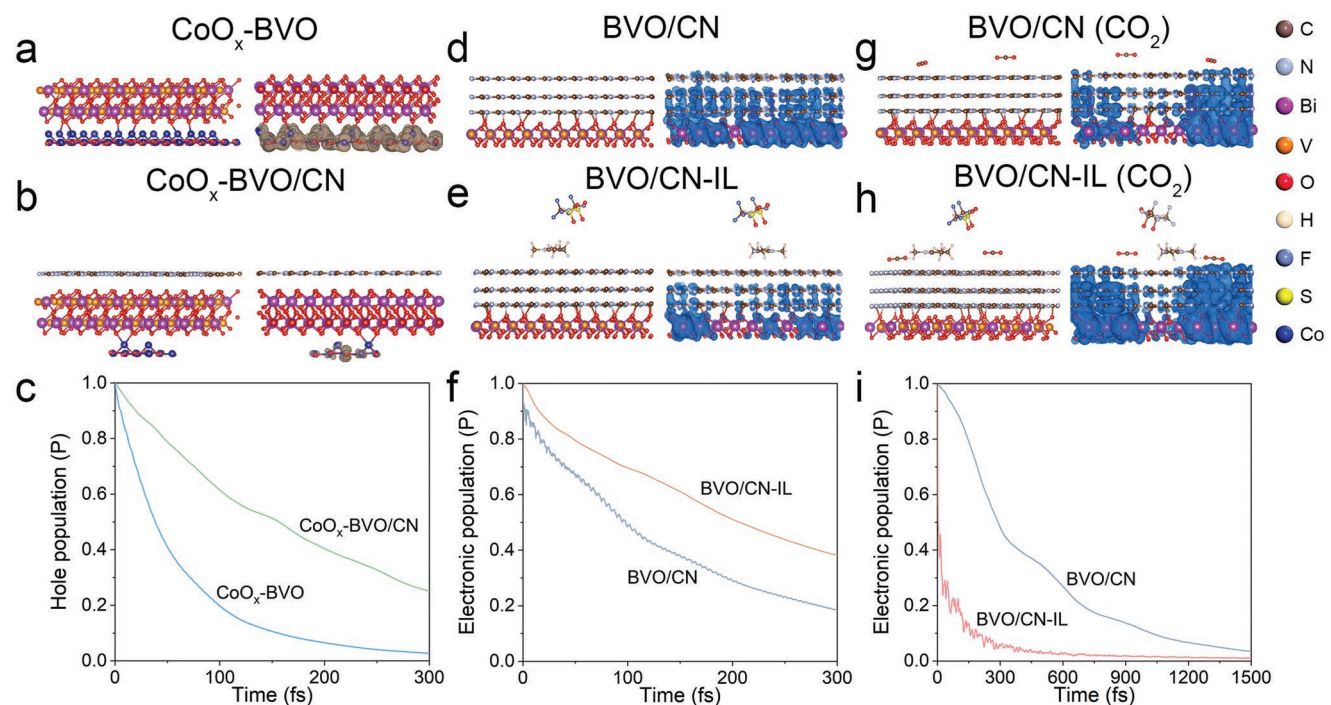


Figure 4. a,b) Graphical representations of the interfacial geometries (left) and the wave function profiles after the electron transfer processes (right) of $\text{CoO}_x\text{-BVO}$ and $\text{CoO}_x\text{-BVO/CN}$. c) The time-dependent survival probability curves of the induced holes during the interfacial electron transfer processes based on the nonadiabatic semiclassical quantum dynamics calculation corresponding to heterostructures of $\text{CoO}_x\text{-BVO}$ and $\text{CoO}_x\text{-BVO/CN}$. Graphical representations of the interfacial geometries (left) and the wave function profiles after the electron transfer processes (right) of BVO/CN and BVO/CN-IL d,e) and after the introduction of CO_2 g,h). The time-dependent survival probability curves of the excited electrons during the interfacial electron transfer processes based on the nonadiabatic semiclassical quantum dynamics calculation corresponding to heterostructures of BVO/CN and BVO/CN-IL f) and i) in the presence of CO_2 .

transfer character of BVO/CN is greatly facilitated after the decoration of IL, especially for the electrons overcoming the limitation of the inner layer for CN and then concentrating on its outer layer. This demonstrates that the modified IL has a powerful induction effect to capture electrons in such a CO_2 enrichment microenvironment. Additionally, it is noticed that the CO_2 molecule could bend at the interface between IL and CN, and an apparent interaction of CO_2 with the electrons is observed in this case (Figure 4h; Figures S30 and S31, Supporting Information). Meanwhile, the H atom of IL is connected to CO_2 with a weak H-bonding character. Hence, the charge transfer of BVO/CN is significantly promoted after IL modification, presenting a transfer curve characterized by a quadratic function, and the total amount of electrons are transferred much faster than that of BVO/CN (Figure 4i). The above results unambiguously reveal that the modified IL could effectively trap electrons and activate CO_2 in the presence of CO_2 .

2.4. Electron Dynamics for CO_2 Reduction

To dive into an in-depth understanding of the reaction kinetics as well as to elucidate the roles of the introduced CoO_x and IL for CO_2 reduction, TAS curves at μs timescale were conducted to determine the charge carrier dynamics of the resulting photocatalysts.^[42] As depicted in Figure 5a, CN yields a broad absorption spanning from 600 to 900 nm under photoexcitation,

and a relatively stronger absorption intensity is observed at 800 nm. While considering the best signal-to-noise ratio, the kinetic traces were probed at 900 nm instead. In order to determine the electron nature of the excited states, the TAS spectra of CN were first measured with and without triethanolamine (TEOA), as a well-known efficient hole scavenger for long-lived electrons. As shown in Figure S32 (Supporting Information), in the presence of TEOA, an increase in half-life time ($t_{50\%}$) compared to that without TEOA is detected on CN. Accordingly, the broad signal observed at 900 nm is assigned to the photogenerated electrons in CN, and this is consistent with the previous observations on C_3N_4 .^[43-44] In comparison, the change in collected probe light is 0.08% for CN, while it is 0.0125% for BVO (Figure S33, Supporting Information). Besides, since CN is the main body in the heterojunctions, it could be deduced that the recorded TAS signal at 900 nm is predominantly from CN, and the main feature observed for photoelectrons localized in CN on BVO/CN heterojunction remains.

One can see that the $t_{50\%}$ of the electron signal increases from 12.6 μs in CN to 25.1 μs in BVO/CN (Figure 5b) under N_2 atmosphere, and a much obvious increase in $t_{50\%}$ is detected on $\text{CoO}_x\text{-BVO/CN}$ (101.2 μs). However, the $t_{50\%}$ of CoO_x -modified CN ($\text{CoO}_x\text{-CN}$) is determined to be only 18.9 μs (Figure S34, Supporting Information). These clearly prove the lifetime of photogenerated electrons on CN is greatly prolonged by the promoted Z-scheme charge transfer between BVO and CN

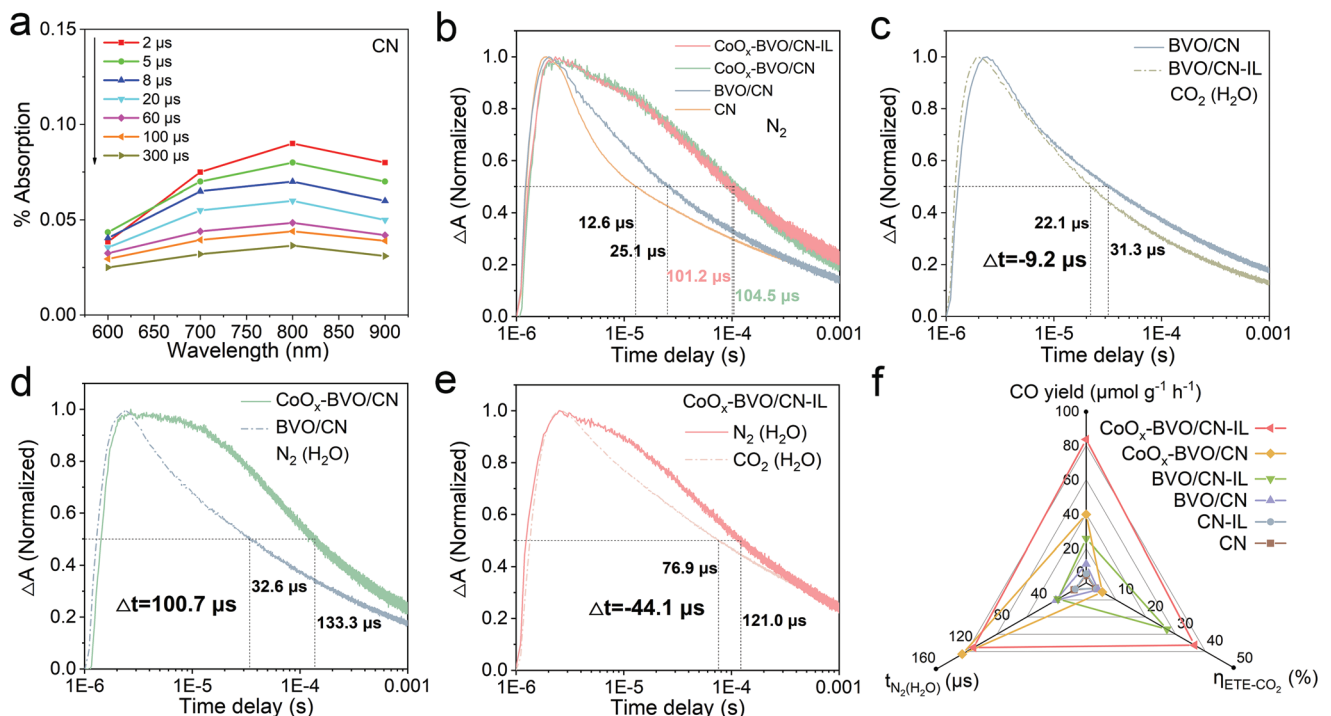


Figure 5. a) μ -TAS spectra of CN in water, b) μ -TAS decay kinetics of CN, BVO/CN, CoO_x-BVO/CN and CoO_x-BVO/CN-IL in N₂, c) μ -TAS decay kinetics of BVO/CN and BVO/CN-IL in CO₂(H₂O) condition, d) μ -TAS decay kinetics of BVO/CN and CoO_x-BVO/CN in N₂(H₂O) condition, e) μ -TAS decay kinetics of CoO_x-BVO/CN-IL in different atmospheres, f) plots on relationships of half-life time ($t_{50\%}$), electron transfer efficiencies (ETE) and CO yields of the investigated samples.

after CoO_x decoration. Whereas, the variations of $t_{50\%}$ (3.3 μ s) observed on CoO_x-BVO/CN-IL are relatively small in contrast to CoO_x-BVO/CN under an N₂ atmosphere. Moreover, in situ investigation of electron kinetics was conducted under simulated photocatalytic CO₂ reduction conditions, in which CO₂(g) carrying H₂O (CO₂(H₂O) for short) was introduced into the test system. For comparison, the measurement was performed by substituting CO₂ with N₂ as well. Figure 5c shows the μ -TAS decay kinetics of BVO/CN and IL modified one. The electron $t_{50\%}$ in BVO/CN-IL is shortened by 9.2 μ s compared with that of BVO/CN in the condition of CO₂(H₂O). Given that the electron $t_{50\%}$ variation between these two samples in N₂(H₂O) are quite small (Figure S35, Supporting Information), it is demonstrated that the IL modification is beneficial for accelerating the electron kinetics for CO₂ reduction in such a CO₂-enriched environment. On the other hand, the electron $t_{50\%}$ in BVO/CN is dramatically prolonged (from 32.6 to 133.3 μ s) after CoO_x decoration in N₂(H₂O) system (Figure 5d), in stark contrast to the variation in those of N₂ (from 25.1 to 104.5 μ s). The results verify the promoted water oxidation kinetics from the vital role of CoO_x by extracting holes and then activating water, contributing to the long-lived electrons accumulated in CN. In addition, one can see the $t_{50\%}$ observed on CoO_x-BVO/CN in the CO₂(H₂O) condition is shortened only by 7.2 μ s compared with that of N₂ filled one (Figure S36, Supporting Information). However, a much obvious variation (44.1 μ s) at the shortened electron lifetime in CoO_x-BVO/CN-IL is recorded (Figure 5e), indicating the modified IL has a rather great effect on CO₂ activation, compared with CoO_x. To make it clear, the electron

transfer efficiency (ETE) for CO₂ reduction is expressed by the following equation:^[45]

$$\eta = 1 - \frac{t_{50\%}(\text{CO}_2)}{t_{50\%}(N_2)} \quad (1)$$

The ETEs for CO₂ reduction of the investigated samples (Table S3, Figures S37–S39, Supporting Information) are calculated, and the plots on relationships of half-life time ($t_{50\%}$), ETE, and CO yields are shown in Figure 5f. One can see the calculated ETE of CN is 3.1% and a tiny increase to 3.4% is acquired on CN-IL, while the ETE for BVO/CN-IL reaches up to 27.1%, indicating the electron capture by CO₂ is facilitated by the modified IL, especially for the Z-scheme heterojunction with long lifetime electrons. This result also supports the fact that IL could serve as a good catalytic activation site for CO₂ reduction. An interesting finding is that, even though the calculated ETE of BVO/CN-IL is higher than that of CoO_x-BVO/CN, a reverse case is observed on the photocatalytic activity, along with the $t_{50\%}$ detected in condition of N₂(H₂O), which is probably due to more electrons reserved on CoO_x-BVO/CN for initiate CO₂ reduction reactions. It should be pointed out here that the ETE for CO₂ reduction reflects the catalysis based on a certain electron lifetime, while the photoactivity comprehensively depends on the ETE value and possibly transferred electrons quantity determined by the electron lifetime. Thus, it can be understood that the maximum ETE reaches 36.4% on CoO_x-BVO/CN-IL, which is related to the remarkably prolonged electron lifetime of CN in BVO/CN Z-scheme heterojunction after CoO_x decoration and to the catalysis of modified ILs for CO₂ reduction, and

the relatively long-lived electrons would bring more profitable conditions for IL to catalyze CO_2 reduction. From another point of view, the electron lifetime observed at 900 nm increases from 32.6 μs in BVO/CN to 121.0 μs in CoO_x -BVO/CN, while the ETE change is small for it is lacking catalysis sites, leading to moderate photoactivity. Therefore, the combination of prolonged electron lifetime and promoted catalysis by means of in situ TAS data is the key to accessing high activity. Obviously, the synergistic effects of modified CoO_x and IL for modulating the Z-scheme charge transfer and activating water and CO_2 boost overall CO_2 reduction reactions.

2.5. Catalysis and Conversion Processes

Electrochemical measurements were also conducted to confirm the role of CoO_x and IL in the resulting Z-scheme heterojunction. One can see the onset potentials of CN and BVO/CN for

electrochemical oxidation are basically identical in the N_2 -bubbled system, while a much lower potential is observed on CoO_x -BVO/CN heterojunction (Figure 6a), manifesting the activation barriers for water oxidation is greatly reduced due to the incorporation of CoO_x . As for the reduction curves performed in the CO_2 -saturated electrolyte (Figure 6b), BVO/CN-IL exhibits the lowest onset potential among the three investigated samples, and it is much lower than that in N_2 -saturated case (Figure S40, Supporting Information), turning out the IL modification is favorable for CO_2 activation. Moreover, in situ diffuse reflectance infrared Fourier transform spectra (DRIFTS) were performed to monitor the variation of the adsorbed reaction molecules and the possible intermediates during CO_2 reduction. As depicted in Figure 6c, the peaks detected at 2338 and 2360 cm^{-1} match with the asymmetric stretching vibration modes of $\text{O}=\text{C}=\text{O}$ for CO_2 ,^[46] and it can be seen that the CO_2 adsorption bands are essentially the same over CN, BVO/CN and CoO_x -BVO/CN heterojunction in the dark, whereas the

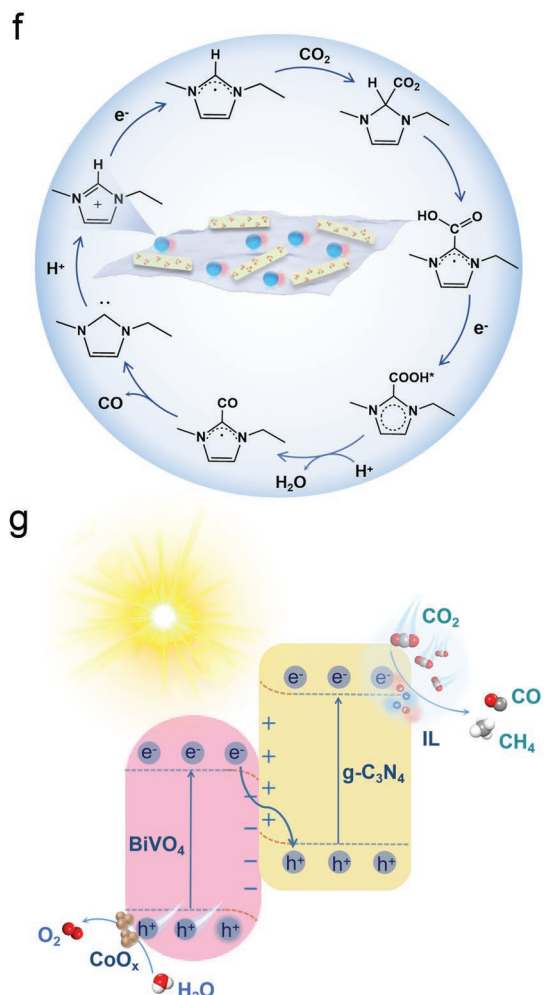
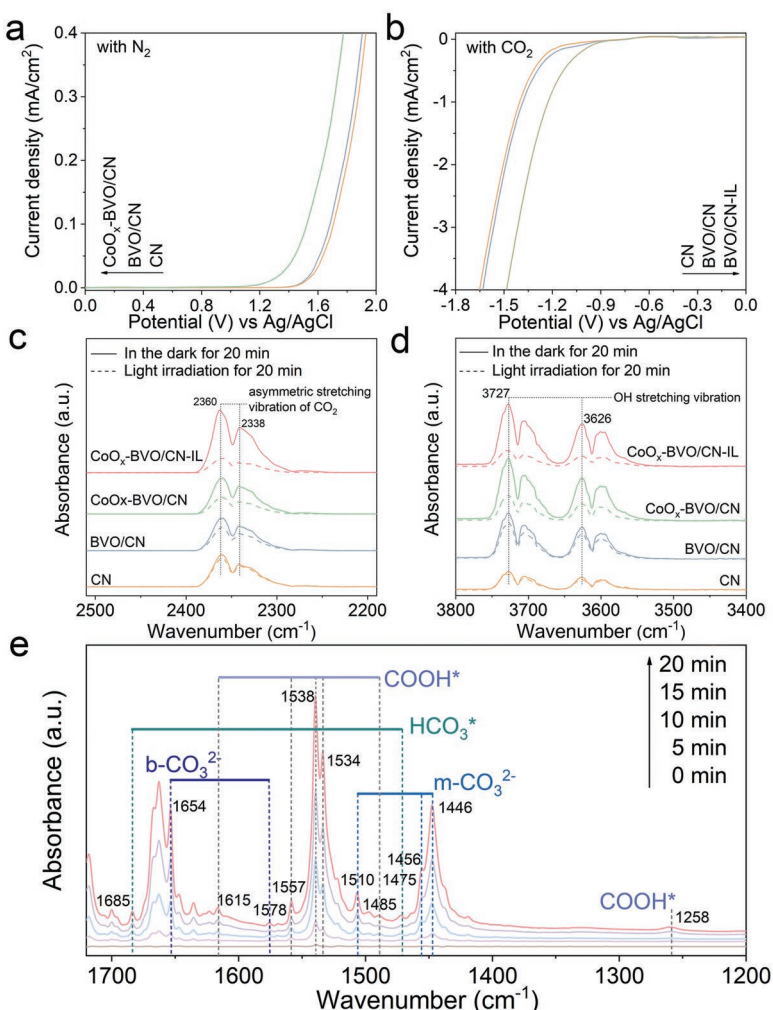


Figure 6. a) Electrochemical oxidation curves of CN, BVO/CN and CoO_x -BVO/CN in an N_2 -saturated electrolyte, b) Electrochemical reduction curves of CN, BVO/CN and BVO/CN-IL in the CO_2 -saturated electrolyte. In situ DRIFTS for adsorbed c) CO_2 c) and d) H_2O in the dark for 20 min and under light irradiation for 20 min of CN, BVO/CN, CoO_x -BVO/CN, and CoO_x -BVO/CN-IL. e) In situ DRIFTS for the detected intermediates of CoO_x -BVO/CN-IL in course of the light irradiation, f) Proposed mechanistic pathway for the CO_2 reduction reaction catalyzed by IL, g) Schematic of the charge transfer and the involved redox reactions on CoO_x -BVO/CN-IL.

intense bands with much stronger stretching vibration of CO₂ is distinguished on IL-containing sample, which is assigned to the formation of strongly adsorbed CO₂ species, implying the modified IL is quite beneficial for CO₂ adsorption. This result is in line with the previous report that CO₂ is apt to complex with C-2 hydrogen of the imidazolium cation.^[47] On the other aspect, the absorption bands (ranging from 3590 to 3730 cm⁻¹) assigned to the joint stretching vibration coupling the H-bound hydroxyl groups with the adsorbed water^[48] are noticed on the investigated samples. The detected signal on BVO/CN is stronger than that of CN, and it is further strengthened after CoO_x decoration.

Intriguingly, the O–H stretching is retained with the subsequent modification of IL, suggesting H₂O molecules are easily adsorbed on CoO_x, rather than IL (Figure 6d). It is worth noting that the CO₂ adsorption bands of CoO_x-BVO/CN are weakened under light irradiation, and it is much more obvious on CoO_x-BVO/CN-IL, yet such variations on CN are quite small. The changes for O–H stretching under light illumination follow the same trends as that of adsorbed CO₂, indicating the modified CoO_x and IL synergistically accelerate the procedure of CO₂ conversion with a more obvious effect of modified IL. One can readily see several new infrared peaks appear and their intensities gradually increase with the extension of irradiation time to 20 min (Figure 6e). The absorption peaks located at 1510, 1456, and 1446 cm⁻¹ belong to m-CO₃²⁻, and the peaks at 1654 and 1578 cm⁻¹ are ascribed to b-CO₃²⁻.^[49–50] While those at 1685 and 1475 cm⁻¹ are attributed to HCO₃^{*}.^[51] Most importantly, the intensities of detected peaks at 1615, 1557, 1538, 1534, and 1485 cm⁻¹ assigned to COOH^{*} groups are strengthened with the prolonged irradiation time, which is generally regarded as the key intermediates for CO₂ reduction to CO,^[52,53] and the results are further disclosed by their typical peaks at \approx 1250 cm⁻¹.^[54]

In light of the combination of in situ TAS and in situ DRIFTS results, a possible CO₂ conversion pathway on the fabricated CoO_x-BVO/CN-IL heterojunction is proposed (Figure 6f). Initially, the imidazolium cation is reduced to generate a neutral radical. Then CO₂ molecules complex with the C-2 hydrogen in the radical to form an imidazolium carboxylate intermediate. Subsequently, the intermediates could be further attacked by the photogenerated electrons to form COOH^{*} species. After that, the produced COOH^{*} would be further protonated to yield CO^{*}, followed by desorption of CO^{*} from the catalyst as the ultimate step. Furthermore, the imidazolium radical could be regenerated to the imidazolium cocatalyst in the presence of a proton source from water.^[55] During photocatalytic CO₂ reduction, when BVO and CN are excited simultaneously, the photogenerated electrons of BVO recombine with the photogenerated holes of CN obeying the Z-scheme charge transfer pathway. The spatially separated photoholes in the VB of BVO would be rapidly extracted by the decorated CoO_x nanoclusters and hence extremely facilitates Z-scheme charge transfer, meanwhile accelerating the water oxidation procedure to produce O₂. On the other hand, the modified IL creates a micro-environment of CO₂ enrichment and then activates CO₂ reduction to CO and CH₄. There is no denying that the constructed spatially-separated redox catalytic sites on CoO_x and IL play crucial roles in synergistically regulating the Z-scheme charge transfer along with the accelerated water oxidation and hence

CO₂ reduction kinetics (Figure 6g). Obviously, this seems like a natural photosynthesis process. To explore the universality of such a strategy, we have also constructed a series of CoO_x and IL co-modified CN-based Z-scheme heterojunctions with the identical method by replacing BVO with other OPs (e.g., Fe₂O₃ and WO₃, structural characterizations depicted in Figures S41 and S42, Supporting Information). One can see that the photocatalytic activities for CO₂ reduction of the fabricated CN-based Z-scheme heterojunctions (Fe₂O₃/CN and WO₃/CN) are greatly improved after CoO_x introduction, and a much higher CO₂ conversion rate is obtained with further decoration of IL (Figure S43, Supporting Information). Besides, similar results on charge separation properties are observed as well (Figure S44, Supporting Information). All these findings undoubtedly demonstrate the versatility of the proposed strategy on synergistically extracting the charge carriers and simultaneously providing catalytic functions by precise construction of spatially separated redox active sites on the fabricated Z-scheme heterojunction for highly efficient solar-driven CO₂ conversion.

3. Conclusions

In summary, BVO/CN Z-scheme heterojunction has been presented as a prototype to show the spatially separated dual site engineering for efficient charge extraction and cocatalysis toward CO₂ photoreduction. The boosted CO₂ conversion is attributed to efficient Z-scheme charge transfer and subsequently the prominent redox co-catalysis by CoO_x and IL respectively for holes-H₂O oxidation and electrons-CO₂ reduction, as proved mainly by means of in situ techniques. Interestingly, the optimal CoO_x-BVO/CN-IL delivers an \approx 80-fold CO production rate without H₂ evolution compared with urea-C₃N₄ counterpart, along with the ETE for CO₂ reduction of 36.4% as revealed by in situ μ -TAS quantitatively. Meanwhile, the fact that high photocatalytic activities of CoO_x-BVO/CN-IL heterojunctions are synergistically dependent on the ETE and possibly transferred electron quantity has also been unraveled. Besides, a CO₂ conversion pathway is proposed, namely, the CO₂ molecules tend to complex with the hydrogen atom of the imidazolium cation to form carboxylate intermediates and then attacked by the photogenerated electrons to form COOH^{*} species to yield CO. This work highlights the synergy of the cascade Z-scheme charge transfer and the precise introduction of individual redox catalytic sites for water and CO₂ activation, and also provides a universal strategy for designing such comprehensive Z-scheme heterojunctions for solar-to-fuel production.

4. Experimental Section

Synthesis of Hydroxylated C₃N₄ Nanosheets (CN): Hydroxylated C₃N₄ nanosheet was prepared by a modified method based on a previous report.^[32] In a typical synthesis, 1 g of melamine and 1.2 g of phosphoric acid were dissolved in 100 mL of deionized water under vigorous magnetic stirring at 80 °C in a water bath. Then the mixture was transferred into a 100 mL Teflon-lined autoclave, sealed, and heated at 180 °C for 10 h. The resulting products were washed with deionized water for several times and dried at 60 °C in an oven. Afterward, 0.6 g

of the prepared powder was refluxed with a mixed aqueous solution of 5 mL glycerol and 15 mL ethanol for 3 h at 90 °C. Then, the obtained products were washed with ethanol for several times and dried at 60 °C. Subsequently, the resultant solids were heated to 500 °C in a muffle furnace with a heating rate of 2 °C min⁻¹ for 2 h. To obtain the hydroxylated C₃N₄ nanosheet, the above few layers C₃N₄ were immersed in HNO₃ solution and refluxed boiling at 130 °C for 6 h followed by washing with water until neutralize the solution, which was dried in an oven. This sample was represented as CN.

Synthesis of BiVO₄ Nanosheets (BVO): In a typical synthesis, 2.21 g of BiCl₃ and 1.05 g of cetyltrimethylammonium bromide (CTAB) were dissolved in 60 mL of ethylene glycol under vigorous magnetic stirring. Then, 2.80 g of NaVO₃ was added to the above solution followed by stirring for 30 min. Then, the mixture was transferred into a 50 mL Teflon-lined autoclave, sealed, and heated at 120 °C for 12 h. After the system was cooled down to room temperature, the resulting products were washed with ethanol and deionized water for several times, and then dried at 60 °C in a vacuum oven. Finally, the obtained sample was fast calcined for 8 min at 400 °C and represented as BVO.

Synthesis of BVO/CN Heterojunction: The CN-coupled BVO was prepared by the hydroxyl-induced assembly method. In the typical synthesis, the desired amounts of CN and BVO were dispersed in 60 mL of aqueous ethanol, and ultrasound for 30 min. Then the above mixture was refluxed at 80 °C for 2 h. Afterward, the obtained samples were washed with deionized water several times and dried at 60 °C in an oven. The obtained samples were named as xBVO/CN heterojunctions, where x (20, 50, and 70) was determined by the mass ratio percentage of BVO to CN.

Synthesis of CoO_x-BVO/CN Heterojunction: The CoO_x-BVO/CN heterojunction was fabricated by a photohole-induced selective deposition method. Specifically, a proper amount of Co₂(CO)₈ was dissolved in a mixture of 10 mL ethanol and 2 mL hexane. 0.1 g of BVO/CN heterojunction was dispersed in 20 mL of aqueous ethanol, and followed by continuous stirring under Ar protection at 40 °C for 30 min. Then, the Co₂(CO)₈ solution was slowly injected into the above suspension and kept stirring for 2 h at 40 °C to allow the Co source fully adsorbed on the surface of the heterojunction. Subsequently, the reaction system was irradiated with a Xenon lamp equipped with a filter ($\lambda \geq 420$ nm) for 2 h. Afterward, the obtained samples were washed with ethanol for several times to remove the dissociative Co source or weakly attached on CN surface ones and then dried at 60 °C in an oven. The obtained sample was named as yCoO_x-BVO/CN, where y (0.1, 0.2, and 0.3) is determined by the mass ratio percentage of CoO_x to BVO.

Synthesis of CoO_x-BVO/CN-IL: A proper volume of 1-ethyl-3-methylimidazolium bis((trifluoromethyl)sulfonyl)imide ([EMIM]NTf₂) was dissolved in 10 mL of methanol. Then, 0.3 g CoO_x-BVO/CN heterojunction was added to the solution with ultrasonic treatment and stirred for 10 min. Afterward, the slurry was treated at 80 °C in a vacuum oven for 12 h. The obtained sample was named as CoO_x-BVO/CN-mIL, where m (5, 10, and 15) was determined by the mass ratio percentage of IL to CN. Characterizations and photocatalytic CO₂ conversion evaluation could be seen in Supporting Information.

Supporting Information

Supporting Information is available from the Wiley Online Library or from the author.

Acknowledgements

L.S. and Z.Q.Z. contributed equally to this work. This work was financially supported by the National Natural Science Foundation of China (no. U1805255, U2102211, 22105066, 22202064). Prof. Yu Zhou, Nanjing Tech University and Panzhe Qiao, Shanghai Advanced Research Institute were acknowledged for their generous support.

Conflict of Interest

The authors declare no conflict of interest.

Data Availability Statement

The data that support the findings of this study are available from the corresponding author upon reasonable request.

Keywords

g-C₃N₄ heterojunction, CO₂ conversions, dual redox sites, electron kinetics, Z-schemes

Received: January 3, 2023

Revised: February 3, 2023

Published online: April 2, 2023

- [1] J. Li, H. Huang, W. Xue, K. Sun, X. Song, C. Wu, L. Nie, Y. Li, C. Liu, Y. Pan, H. Jiang, D. Mei, C. Zhong, *Nat. Catal.* **2021**, *4*, 719.
- [2] Y. Hao, L. Chen, J. Li, Y. Guo, X. Su, M. Shu, Q. Zhang, W. Gao, S. Li, Z. Yu, L. Gu, X. Feng, A. Yin, R. Si, Y. Zhang, B. Wang, C. Yan, *Nat. Commun.* **2021**, *12*, 2682.
- [3] L. Liu, M. Li, F. Chen, H. Huang, *Small Struct.* **2022**, 2200188.
- [4] W. Tu, Y. Yang, C. Chen, T. Zhou, T. Li, H. Wang, S. Wu, Y. Zhou, D. O'Hare, Z. Zou, R. Xu, *Small Struct.* **2022**, 2200233.
- [5] L. Lin, Z. Lin, J. Zhang, X. Cai, W. Lin, Z. Yu, X. Wang, *Nat. Catal.* **2020**, *3*, 649.
- [6] F. Guo, B. Hu, C. Yang, J. Zhang, Y. Hou, X. Wang, *Adv. Mater.* **2021**, *33*, 2101466.
- [7] X. Chen, J. Wang, Y. Chai, Z. Zhang, Y. Zhu, *Adv. Mater.* **2021**, *33*, 2007479.
- [8] S. Wang, X. Han, Y. Zhang, N. Tian, T. Ma, H. Huang, *Small Struct.* **2021**, *2*, 2000061.
- [9] W. Zhang, A. Mohamed, W. Ong, *Angew. Chem., Int. Ed.* **2020**, *59*, 22894.
- [10] Y. Wang, X. Shang, J. Shen, Z. Zhang, D. Wang, J. Lin, J. Wu, X. Fu, X. Wang, C. Li, *Nat. Commun.* **2020**, *11*, 3043.
- [11] Q. Gao, J. Xu, Z. Wang, Y. Zhu, *Appl. Catal. B* **2020**, *271*, 118933.
- [12] Z. Pan, G. Zhang, X. Wang, *Angew. Chem., Int. Ed.* **2019**, *58*, 7102.
- [13] Z. Mu, S. Chen, Y. Wang, Z. Zhang, Z. Li, B. Xin, L. Jing, *Small Sci.* **2021**, *1*, 2100050.
- [14] J. Bian, Z. Zhang, J. Feng, M. Thangamuthu, F. Yang, L. Sun, Z. Li, Y. Qu, D. Tang, Z. Lin, F. Bai, J. Tang, L. Jing, *Angew. Chem., Int. Ed.* **2021**, *60*, 20906.
- [15] Q. Xu, L. Zhang, B. Cheng, J. Fan, J. Yu, *Chem* **2020**, *6*, 1543.
- [16] C. T. K. Nguyen, N. Q. Tran, S. Seo, H. Hwang, S. Oh, J. Yu, J. Lee, T. A. Le, J. Hwang, M. Kim, H. Lee, *Mater. Today* **2020**, *35*, 25.
- [17] Y. Qi, J. Zhang, Y. Kong, Y. Zhao, S. Chen, D. Li, W. Liu, Y. Chen, T. Xie, J. Cui, C. Li, K. Domen, F. Zhang, *Nat. Commun.* **2022**, *13*, 484.
- [18] P. Wang, P. Fu, J. Ma, Y. Gao, Z. Li, H. Wang, F. Fan, J. Shi, C. Li, *ACS Catal.* **2021**, *11*, 12736.
- [19] X. Yu, Z. Yu, X. Zhang, P. Li, B. Sun, X. Gao, K. Yan, H. Liu, Y. Duan, M. Gao, G. Wang, S. Yu, *Nano Energy* **2020**, *71*, 104652.
- [20] R. Li, F. Zhang, D. Wang, J. Yang, M. Li, J. Zhu, X. Zhou, H. Han, C. Li, *Nat. Commun.* **2013**, *4*, 1432.
- [21] S. Cao, B. Shen, T. Tong, J. Fu, J. Yu, *Adv. Funct. Mater.* **2018**, *28*, 1800136.

- [22] H. Wu, X. Kong, X. Wen, S. Chai, E. C. Lovell, J. Tang, Y. H. Ng, *Angew. Chem., Int. Ed.* **2021**, *60*, 8455.
- [23] B. A. Rosen, K. A. Salehi, M. R. Thorson, W. Zhu, D. T. Whipple, P. J. Kenis, R. I. Masel, *Science* **2011**, *334*, 643.
- [24] S. Bi, H. Banda, M. Chen, L. Niu, M. Chen, T. Wu, J. Wang, R. Wang, J. Feng, T. Chen, M. Dirca, A. A. Kornyshev, G. Feng, *Nat. Mater.* **2020**, *19*, 552.
- [25] G. P. S. Lau, M. Schreier, D. Vasilyev, R. Scopelliti, M. Gratzel, P. J. Dyson, *J. Am. Chem. Soc.* **2016**, *138*, 7820.
- [26] S. Wang, X. Wang, *Angew. Chem., Int. Ed.* **2016**, *55*, 2308.
- [27] X. Mao, P. Brown, C. Cervinka, G. Hazell, H. Li, Y. Ren, D. Chen, R. Atkin, J. Eastoe, I. Grillo, A. A. H. Padua, M. F. CostaGomes, T. A. Hatton, *Nat. Mater.* **2019**, *18*, 1350.
- [28] S. Yu, P. K. Jain, *Nat. Commun.* **2019**, *10*, 2022.
- [29] S. Zhang, J. Zhang, Y. Zhang, Y. Deng, *Chem. Rev.* **2017**, *117*, 6755.
- [30] C. Cheng, B. He, J. Fan, B. Cheng, S. Cao, J. Yu, *Adv. Mater.* **2021**, *33*, 2100317.
- [31] Y. Zhang, J. Zhao, H. Wang, B. Xiao, W. Zhang, X. Zhao, T. Lv, M. Thangamuthu, J. Zhang, Y. Guo, J. Ma, L. Lin, J. Tang, R. Huang, Q. Liu, *Nat. Commun.* **2022**, *13*, 58.
- [32] Y. Xiao, G. Tian, W. Li, Y. Xie, B. Jiang, C. Tian, D. Zhao, H. Fu, *J. Am. Chem. Soc.* **2019**, *141*, 2508.
- [33] L. Lin, Z. Yu, X. Wang, *Angew. Chem., Int. Ed.* **2019**, *58*, 6164.
- [34] K. Zhang, B. Jin, C. Park, Y. J. Cho, X. Song, X. Shi, S. Zhang, W. Kim, H. Zeng, J. H. Park, *Nat. Commun.* **2019**, *10*, 200.
- [35] C. Lv, Y. Qian, C. Yan, Y. Ding, Y. Liu, G. Chen, G. Yu, *Angew. Chem., Int. Ed.* **2018**, *57*, 10246.
- [36] T. Cremer, M. Killian, J. M. Gottfried, N. Paape, P. Wasserscheid, F. Maier, H. P. Steinruck, *ChemPhysChem* **2008**, *9*, 2185.
- [37] B. Wu, L. Zhang, B. Jiang, Q. Li, C. Tian, Y. Xie, W. Li, H. Fu, *Angew. Chem., Int. Ed.* **2021**, *60*, 4815.
- [38] L. Zhai, X. She, L. Zhuang, Y. Li, R. Ding, X. Guo, Y. Zhang, Y. Zhu, K. Xu, H. Fan, S. Lau, *Angew. Chem., Int. Ed.* **2022**, *61*, 202116057.
- [39] C. Jiang, J. Yang, T. Zhao, L. Xiong, Z. Guo, Y. Ren, H. Qi, A. Wang, J. Tang, *Appl. Catal. B* **2021**, *282*, 119571.
- [40] K. Shah, R. Dai, M. Mateen, Z. Hassan, Z. Zhuang, C. Liu, M. Israr, W. Cheong, B. Hu, R. Tu, C. Zhang, X. Chen, Q. Peng, C. Chen, Y. Li, *Angew. Chem., Int. Ed.* **2022**, *61*, 202114951.
- [41] J. Qi, Y. Lin, D. Chen, T. Zhou, W. Zhang, R. Cao, *Angew. Chem., Int. Ed.* **2020**, *59*, 8911.
- [42] S. Selim, E. Pastor, T. M. Garcia, M. R. Morris, L. Francas, M. Sachs, B. Moss, S. Corby, C. A. Mesa, S. Gimenez, A. Kafizas, A. A. Bakulin, J. R. Durrant, *J. Am. Chem. Soc.* **2019**, *141*, 18791.
- [43] Y. Wang, R. Godin, J. R. Durrant, J. Tang, *Angew. Chem., Int. Ed.* **2021**, *60*, 20811.
- [44] Y. Wang, X. Liu, X. Han, R. Godin, J. Chen, W. Zhou, C. Jiang, J. F. Thompson, K. B. Mustafa, S. A. Shevlin, J. R. Durrant, Z. Guo, J. Tang, *Nat. Commun.* **2020**, *11*, 2531.
- [45] A. K. , K. T. , K. T. , M. K. , P. V. Kamat, *J. Am. Chem. Soc.* **2008**, *130*, 4007.
- [46] P. Yang, R. Wang, H. Tao, Y. Zhang, M. M. Titirici, X. Wang, *Appl. Catal. B* **2021**, *280*, 119454.
- [47] F. Etsuko, C. G. David, F. M. Gerald, E. P. Dmitry, *Acc. Chem. Res.* **2022**, *55*, 616.
- [48] Y. Liu, Y. Li, X. Li, Q. Zhang, H. Yu, X. Peng, F. Peng, *ACS Nano* **2020**, *14*, 14181.
- [49] X. Jiao, X. Li, X. Jin, Y. Sun, J. Xu, L. Liang, H. Ju, J. Zhu, Y. Pan, W. Yan, Y. Lin, Y. Xie, *J. Am. Chem. Soc.* **2017**, *139*, 18044.
- [50] J. Xu, Z. Ju, W. Zhang, Y. Pan, J. Zhu, J. Mao, X. Zheng, H. Fu, M. Yuan, H. Chen, R. Li, *Angew. Chem., Int. Ed.* **2021**, *60*, 8705.
- [51] Y. He, H. Rao, K. Song, J. Li, Y. Yu, Y. Lou, C. Li, Y. Han, Z. Shi, S. Feng, *Adv. Funct. Mater.* **2019**, *29*, 1905153.
- [52] X. Xiong, C. Mao, Z. Yang, Q. Zhang, G. I. N. Waterhouse, L. Gu, T. Zhang, *Adv. Energy Mater.* **2020**, *10*, 2002928.
- [53] Y. Hu, F. Zhan, Q. Wang, Y. Sun, C. Yu, X. Zhao, H. Wang, R. Long, G. Zhang, C. Gao, W. Zhang, J. Jiang, Y. Tao, Y. Xiong, *J. Am. Chem. Soc.* **2020**, *142*, 5618.
- [54] J. Yi, R. Xie, Z. Xie, G. Chai, T. Liu, R. Chen, Y. Huang, R. Cao, *Angew. Chem., Int. Ed.* **2020**, *59*, 23641.
- [55] S. Zhao, M. Horne, A. M. Bond, J. Zhang, *J. Phys. Chem. C* **2016**, *120*, 23989.